Research Article

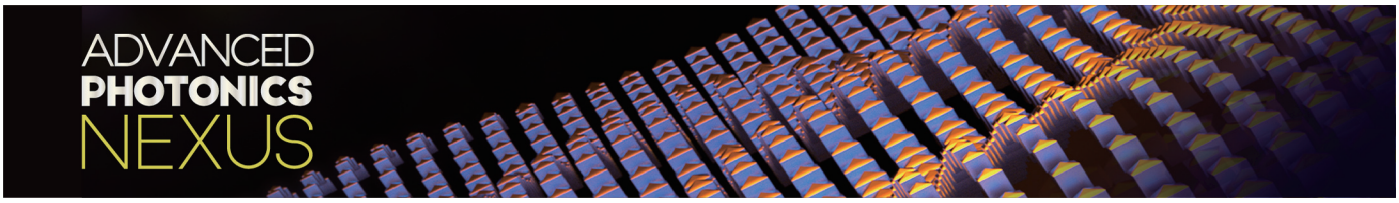

Stable high-peak-power fiber supercontinuum generation for adaptive femtosecond biophotonics

Geng Wang,[a,b] Jindou Shi,[a,b] Rishyashring R. Iyer,[a,b] Janet E. Sorrells,[a,c] and Haohua Tu[a,b,*]
[a]University of Illinois at Urbana-Champaign, Beckman Institute for Advanced Science and Technology, Urbana, Illinois, United States
[b]University of Illinois at Urbana-Champaign, Department of Electrical and Computer Engineering, Urbana, Illinois, United States
[c]University of Illinois at Urbana-Champaign, Department of Bioengineering, Urbana, Illinois, United States

Abstract. Broad and safe access to ultrafast laser technology has been hindered by the absence of optical fiber-delivered pulses with tunable central wavelength, pulse repetition rate, and pulse width in the picosecond–femtosecond regime. To address this long-standing obstacle, we developed a reliable accessory for femtosecond ytterbium fiber chirped pulse amplifiers, termed a fiber-optic nonlinear wavelength converter (FNWC), as an adaptive optical source for the emergent field of femtosecond biophotonics. This accessory empowers the fixed-wavelength laser to produce fiber-delivered ~20 nJ pulses with central wavelength across 950 to 1150 nm, repetition rate across 1 to 10 MHz, and pulse width across 40 to 400 fs, with a long-term stability of >2000 h. As a prototypical label-free application in biology and medicine, we demonstrate the utility of FNWC in real-time intravital imaging synergistically integrated with modern machine learning and large-scale fluorescence lifetime imaging microscopy.

Keywords: femtosecond biophotonics; fiber supercontinuum; label-free multiphoton microscopy; nonlinear optics and imaging; self-supervised denoise.

Received Apr. 20, 2024; revised manuscript received May 23, 2024; accepted for publication Jun. 27, 2024; published online Jul. 17, 2024.

[DOI: 10.1117/1.APN.3.4.046012]

1 Introduction

Ultrafast laser engineering has produced mode-locked optical pulses with (sub-) picosecond duration (τ) at a megahertz-level repetition rate (f)[1] and driven the broad field of femtosecond biophotonics.[2] These ultrashort pulses were first produced six years after the invention of the laser.[3] Subsequently, the Ti:sapphire crystal was recognized as a better lasing medium than dye solutions to support a broad range of near-infrared wavelengths (λ).[4] The revolutionary development of Kerr lens mode locking in 1990[5] led to the commercialization of high average power (P) Ti:sapphire lasers tunable across 690 to 1020 nm. More recent innovation around 2010 resulted in an ytterbium-based optical parametric oscillator (OPO) with one output widely tunable across 680 to 1300 nm and another synergistic output fixed at ~1040 nm.[6] Today, automatic wavelength tuning, beam pointing correction, and dispersion compensation have enabled many aspects of femtosecond biophotonics, including biological microscopy or clinical imaging,[7] nanosurgery,[8] and optogenetics.[9] However, despite decades of development in solid-state ultrafast sources, it remains technically challenging to tune the three pulse parameters of λ, f, and τ independently and widely with sufficient output (P) or pulse energy (E). In particular, the typical inability to vary f not only limits the solid-state ultrafast lasers themselves, but also the subsequent wavelength-tuning accessories of the optical parametric amplifier (OPA).

In contrast to the solid-state lasers, ultrafast fiber lasers have played a relatively minor role in femtosecond biophotonics despite their rapid advances,[10] largely due to the difficulty of tuning λ (and to a lesser degree, τ toward shorter durations). The fiber chirped pulse amplification (FCPA)[11] of a pulse-picked seed along a large-core ytterbium (Yb) gain fiber, which could be either a conventional circular fiber or a largely single-mode photonic crystal fiber, such as DC-200/40-PZ-Yb (NKT Photonics),[12] has led to various commercial FCPA lasers (Table S1 in the Supplementary Material) useful for LASIK

*Address all correspondence to Haohua Tu, htu@illinois.edu

eye surgery and material processing. These pulse-picked FCPA (PP-FCPA) lasers have an advantage over the solid-state lasers due to the ease of varying f at the same P, i.e., preamplification pulse picking for variable E. It seems that pairing one PP-FCPA laser with an OPA accessory would empower the tuning of λ and τ (Table S1 in the Supplementary Material) to compete favorably with the solid-state lasers. However, the OPA is a largely free-space add-on that diminishes the fiber-optic advantages of the PP-FCPA laser, e.g., high resistance to environmental disturbance and good beam quality ensured by single-mode fiber propagation. Also, routine operation and maintenance of an integrated FCPA-OPA laser is often beyond the expertise of a biologist. Thus the tuning accessory based on OPA technology has limited the application of the otherwise attractive PP-FCPA lasers to compete with their solid-state counterparts. To overcome these OPA-related limitations, we aim to develop an alternative tuning accessory based on the seeding subunit of OPA technology,[13] known as supercontinuum (or white-light) generation.

2 Results

2.1 High-Peak-Power Coherent Fiber Supercontinuum Generation

Bulk-medium supercontinuum generation was demonstrated in glasses using picosecond (ps) pulses.[14] Later, femtosecond (fs) pulses were more useful in the seed generation of commercial OPA operated at 0.25 MHz[15] (Table S2 in the Supplementary Material), which also enabled the commercial OPA accessories of the PP-FCPA lasers toward larger f of ~4 MHz (Table S1 in the Supplementary Material). Interestingly, photonic crystal fiber-based supercontinuum generation was first demonstrated using fs pulses,[16] but ps pulses gained commercial success later due to its robust all-fiber setup[17] [Fig. 1(a), approach 1; Table S2 in the Supplementary Material]. The success of this ps approach in wide spectral broadening has largely restricted the fs approach to an add-on nonlinear wavelength converter for a solid-state Ti:sapphire oscillator [Fig. 1(a), approach 2]. A third approach has diverged from either the all-fiber supercontinuum generation or the solid-state laser, and instead focused on coherent fiber supercontinuum generation[18] by an fs Yb:fiber laser free of the pulse picking and a bare fiber several centimeters (cm) in length[19–21] [Fig. 1(a), approach 3]. Despite this progress, the corresponding nonlinear fibers have a relatively small core (<12 μm) and do not support high-peak-power coherent fiber supercontinuum generation by the PP-FCPA lasers (Table S1 in the Supplementary Material). In this context, our recent attempt using a PP-FCPA laser (Satsuma, Amplitude) and a large-core (15 μm) photonic crystal fiber (LMA-PM-15, NKT Photonics)[22] put us in a position to develop the alternative tuning accessory (Table S2 in the Supplementary Material).

Unfortunately, we found that the corresponding supercontinuum generating fiber inevitably suffered irreversible photodamage after ~100 h of accumulative operation. This disruption prohibits the operation of the corresponding supercontinuum laser by a biologist (without extensive laser training). It is thus important to identify the nature of this long-term photodamage and then avoid it. We aimed to answer whether this photodamage was caused by an airborne contaminant in a nonclean-room environment and/or high-peak-intensity free-space coupling at two fiber end facets, which could be avoided by commercial photonic crystal fiber end-capping/termination with specific hole collapsing and beam expansion[23] [Fig. 1(a), approach 2], or other more complicated mechanisms.

2.2 Experiment on Two Schemes of Fiber Supercontinuum via Approach 3

Our custom-built coherent fiber supercontinuum source [Fig. 1(a), approach 3; Table S3 in the Supplementary Material, Scheme 1] enabled slide-free histochemistry,[22] nonlinear optogenetics,[24] and label-free imaging of extracellular vesicles.[25] The supercontinuum output along one principal axis of polarization-maintaining (PM) LMA-PM-15 fiber with a high polarization extinction ratio (PER) reproducibly exhibited the same spectrum [Fig. 1(b), Scheme 1] for different cleaved 25-cm fiber pieces (Table S3 in the Supplementary Material), as asserted by a deterministic model[26] taking account of the polarization effect.[27] However, each piece encountered long-term photodamage after accumulative (not continuous) operation of 100 h $\pm$ 40 h (20 pieces in total), resulting in gradually reduced (up to 10%) coupling efficiency not compensable by optical realignment along with narrowed spectral broadening and often degraded output beam quality. We observed this fiber photodamage in another polarized supercontinuum source,[28] except for the use of a non-FCPA operated at 40 MHz as the master laser [Fig. 1(a), Approach 3; Table S3 in the Supplementary Material, Scheme 2]. Although Scheme 2 matched Scheme 1 in input peak intensity (Table S3 in the Supplementary Material), the resulting supercontinuum produced a broader spectrum due to the lower dispersion of the fiber [Fig. 1(b), bottom]. However, photodamage with gradually reduced coupling efficiency was found to occur in a shorter time frame of 10 h $\pm$ 2 h (Table S3 in the Supplementary Material), so the stain-free histopathology had to replace the fiber daily to obtain reproducible results.[29] This photodamage required replacement of the fiber with tedious optical realignments and thus limited the femtosecond biophotonics application of both schemes of supercontinuum source.

We identified one key difference between the two schemes. The photodamage in Scheme 2 was localized within 1 cm beyond the entrance end of the fiber, as recleaving this length for a damaged 25-cm fiber piece would recover the fiber coupling efficiency and supercontinuum bandwidth. In contrast, the photodamage in Scheme 1 was relatively delocalized, as re-cleaving up to 10-cm length beyond the entrance end of a damaged 25-cm fiber piece was needed to recover the fiber coupling efficiency. The observed localization of fiber photodamage and reduced coupling efficiency over time are inconsistent with airborne contamination in a nonclean-room environment and/or high-peak-intensity free-space coupling. The former would lead to a rather sudden or random reduction of the coupling efficiency while the latter would lead to spatiotemporally similar photodamage for the two schemes. Thus, it is unlikely to mitigate the photodamage by specific fiber end-capping with mode expansion [Fig. 1(a), Approach 2].

2.3 Test on a Third Scheme of Fiber Supercontinuum Via Approach 3

The observed photodamage in Scheme 2 supports the interpretation based on the emergence of a photoscattering waveguide at the fiber entrance end[30,31] in the form of long-period fiber grating (LPFG).[32] In this interpretation, the input pulse propagating in the core mode beats with the copropagating pulse in a cladding

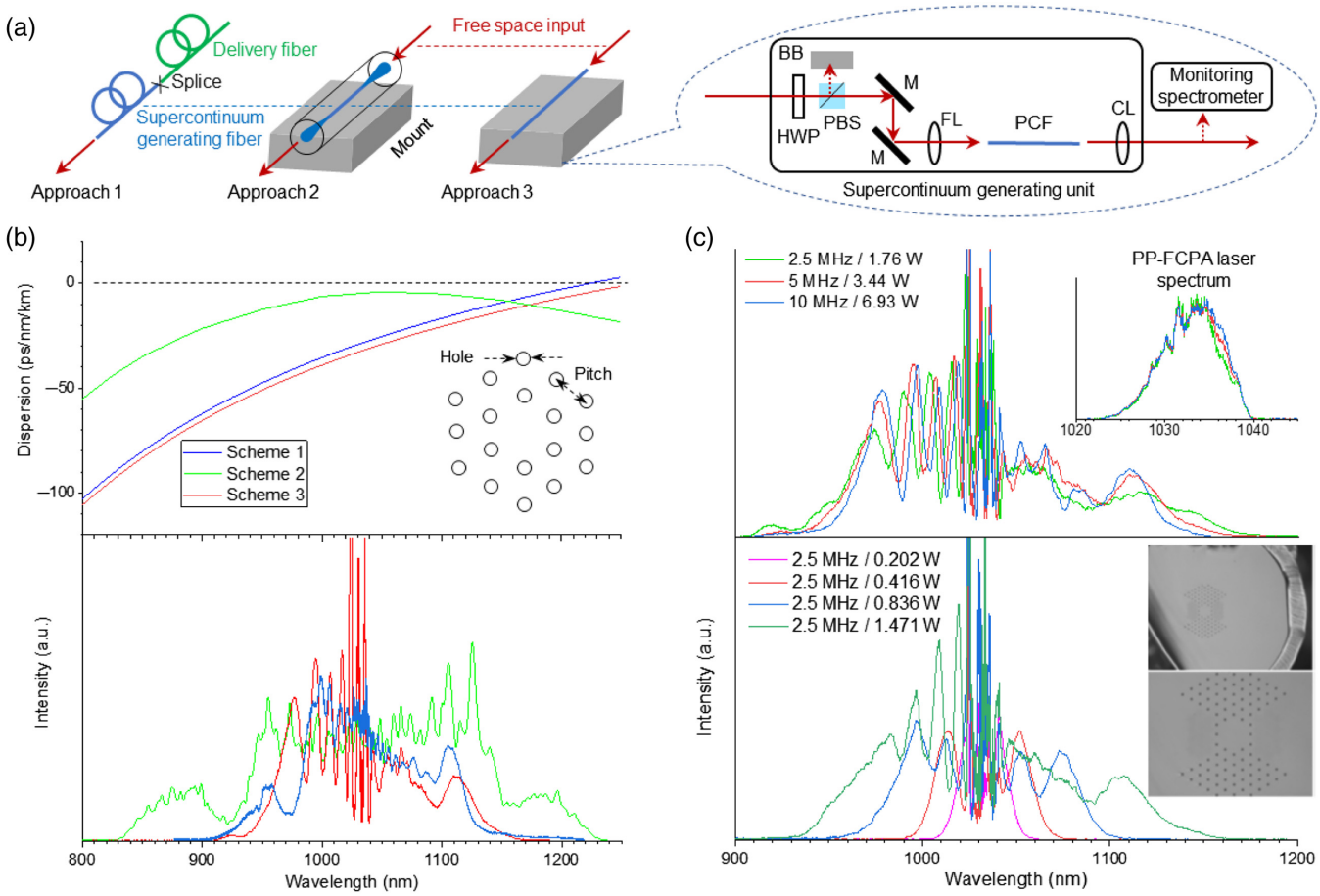

Fig. 1 (a) Three general approaches for fiber supercontinuum generation: all-fiber splice often used in commercial supercontinuum lasers (approach 1), commercial enclosed device with fiber end capping and mode expansion as an add-on nonlinear wavelength converter for a Ti:sapphire oscillator (approach 2), and mounted bare (PM) fiber for coherent fiber supercontinuum generation by an fs Yb:fiber laser (approach 3). PP-FCPA, pulse-picked fiber chirped pulse amplifier; BB, beam blocker; HWP, half-wave plate; PBS, polarizing beam splitter; M, mirror; FL, focusing lens; PCF, photonic crystal fiber; CL, collimating lens. (b) Three schemes of polarized coherent fiber supercontinuum generation under study with wavelength-dependent dispersion of photonic crystal fibers indicative of the restriction of supercontinuum generation to fiber normal dispersion regimes (top) with a cross-sectional image of photonic crystal fibers indicative of pitch and hole sizes (inset), and corresponding spectra of supercontinuum outputs (bottom). (c) Output spectra at different f but the same E for Scheme 3 (top) in comparison with input spectra of source laser (inset), and output spectra at different E but the same f for Scheme 3 (bottom) with cross-sectional images of the supercontinuum generating fiber (inset).

mode after free-space-to-fiber coupling to produce the standing wave that writes and progressively strengthens an LPFG. The period (Λ) of this LPFG is determined by the phase matching of $\Lambda = \lambda/[n_{co}(\lambda) - n_{cl}(\lambda)]$, where λ is the central wavelength of the pulses while $n_{co}(\lambda)$ and $n_{cl}(\lambda)$ are the corresponding effective refractive index of the core mode and cladding mode, respectively. The pulses have broad bandwidths (~10 nm for 280 fs input and larger along the fiber for the core mode due to supercontinuum generation) from which the blue and red edges write slightly different grating periods and lead to the localized LPFG formation at the entrance end (because the superposition of the gratings from different wavelengths can be in phase for a limited length). The temporal walk-off between two pulses may also contribute to this localized LPFG formation.

For a given λ, the period Λ of a circular fiber can be calculated from the dielectric structure of the fiber cross section. [32] Similarly, Λ of a photonic crystal fiber can be calculated from the pitch and hole sizes of the fiber cross section [Fig. 1(b), inset] for the two schemes (Table S3 in the Supplementary Material), if $n_{cl}(\lambda)$ approximates the effective refractive index of the fundamental space filling mode. [33] The much larger Λ in Scheme 1 as opposed to Scheme 2 is thus responsible for more delocalized fiber photodamage to approach similar LPFG strength (with dozens of periods) or loss of fiber coupling efficiency (10%), and slower LPFG formation via increased spectral broadening (supercontinuum generation) and/or pulse walk-off at longer fiber lengths. As a nontrivial prediction from this interpretation, the LPFG-based photodamage would

disappear if the calculated Λ approaches the total length of the supercontinuum-generating fiber (because the LPFG would function poorly with only one period).

To test this prediction, we developed a third scheme of supercontinuum generation using an ultralarge core silica photonic crystal fiber (LMA-PM-40-FUD, NKT Photonics) that approximates the doped DC-200/40-PZ-Yb fiber in a PP-FCPA laser,[12] with a cross section of large-pitch small-hole lattice [Fig. 1(a), approach 3; Table S3 in the Supplementary Material, Scheme 3]. The selection of a short fiber length (9.0 cm) not only avoided an undesirable bending effect[34] or depolarization effect[27] but also approached the calculated Λ from this fiber (Table S3 in the Supplementary Material). The PCF longer than 9 cm does not significantly increase supercontinuum bandwidth but generates a large chirp beyond the range of our prism-based compressor. Without the fiber end capping [Fig. 1(a), approach 2], the resulting supercontinuum source [Fig. 1(b), Scheme 3] remained stable after >2000 h of accumulative operation within 2 years in a regular (nonclean-room) optical laboratory. This test validates our LPFG-based interpretation of fiber photodamage. In addition to the suppression of the LPFG photodamage, the large core size (40 μm) also scales up the peak power for tunable pulse generation (see below), just like that for nondissipative[34] and dissipative soliton pulses.[35]

2.4 Fiber-optic Nonlinear Wavelength Converter

We next examined the dependence of the supercontinuum spectrum [Fig. 1(a), approach 3; Table S3 in the Supplementary Material, Scheme 3] on f of the master PP-FCPA laser at the same pulse energy E (i.e., P/f). The laser/input spectrum and τ were rather independent of f, so that the supercontinuum output retained a similar spectrum across a wide f range of 2 to 10 MHz [Fig. 1(c), top]. This deterministic generation of coherent fiber supercontinuum is not surprising because the spectrum can be theoretically predicted if the spatiotemporal property of the input laser pulse is known.[26] Similar f-independent spectra were obtained at lower E, so that the leftmost and rightmost spectral lobes may be filtered to generate compressed pulses[21] across 950 to 1110 nm, wherein they converge at 1030 nm [Fig. 1(c), bottom]. The observed f-independent supercontinuum generation resembles that of soliton generation.[36]

Experimentally, collimated fiber supercontinuum output was aligned along the horizontal polarization by an achromatic half-wave plate to enter a pulse dispersion compensation unit [Fig. 2(a)] in the form of a programmable pulse shaper (FemtoJock, Biophotonic Solutions), which was empowered by multiphoton intrapulse interference phase scan[37] through a 128-pixel spatial light modulator (SLM).[38] The pulse shaper spectrally selected a fixed-bandwidth window (~60 nm) inside the supercontinuum spectrum with a tunable central wavelength across 950 to 1110 nm after motorized rotation of the reflective grating of the pulse shaper to project this spectral window on the SLM.[39] For a pulse centered at $\lambda = 1030$ nm without the spectral lobe filtering or at a detuned λ (e.g., 1110 nm) with this filtering,[21] the pulse shaper allowed compressing this pulse close to its transform limit τ (~60-fs FWHM or ~40-fs sech^2- shape)[37,39] and chirping/tuning the pulse to 400 fs [Fig. 2(b)].

Optionally, the free-space output from the pulse shaper was recoupled into a 1-m low-dispersion Kagome hollow-core fiber patch cable (PMC-C-Yb-7C, GLOphotonics) by an achromatic lens of 75-mm focal length, with slightly λ-dependent efficiency of 76% ± 3%. The weak birefringence that is intrinsic to the hollow-core fiber[40] allowed rotating the input polarization by a half-wave plate to maximize the PER of fiber-delivered output to 10 to 20, depending on the bending state of the fiber. The spectrum and spatial beam profile of fiber-delivered output after the collimation by an achromatic lens (75-mm focal length) approximated those of the free-space input before the fiber, while the small pulse duration of free-space input was largely retained [Fig. 2(b)]. At the cost of 24% lower P or E and slightly degraded PER, the fiber pulse delivery gains several advantages over free-space pulse delivery. (i) Simple fiber telecommunication connection and disconnection allows easy switching among different optical fiber-coupled application modules, i.e., sharing the fiber delivered output among these modules [Fig. 2(a)]. (ii) Fiber delivery of energetic pulses is safer than free-space delivery for operators without extensive laser training. (iii) The optimal fiber recoupling condition of endless single-mode fiber supercontinuum[41,42] is independent of λ (i.e., rotation of the grating in the pulse shaper), which can be useful to monitor and correct the misalignment of the pulse shaper itself[38] in portable applications of this tunable source (beyond an environmentally controlled laboratory).

The SLM-based pulse shaper is not necessary for the tunable fiber supercontinuum source with or without hollow-core fiber delivery when only tunable-τ pulse generation (rather than arbitrary pulse shaping[39]) is needed. We tested a more cost-effective alternate of single-prism pulse compressor (BOA-1050, Swamp Optics) and generated a similar tunable-λ ~40 fs (sech^2) pulse by motorized rotation of the prism and the linear motion of a back retroreflector that varies group delay dispersion (GDD) (Table S4 in the Supplementary Material), indicating that the chirp of this fixed-bandwidth pulse is largely linear. Due to the fiber input (supercontinuum generation) and optional fiber output (dispersion-free pulse transmission through the hollow-core fiber) of the dispersion compensation unit, we term the whole device a fiber-optic nonlinear wavelength converter (FNWC) [Fig. 2(a), Table S4 in the Supplementary Material]. Our FNWC may be generalized to other PP-FCPA lasers (Table S1 in the Supplementary Material) with f-independent emission spectrum [Fig. 1(c), top]. In contrast to commercial alternatives, such as an OPA or OPO, FNWC can independently and widely tune λ, f, and τ (Tables S4 and S5 in the Supplementary Material).

There is room to further improve the existing FNWC technology. Broader bandwidths of fiber supercontinuum generation at high input powers may be possible if the multimodal behavior at longer wavelengths (>1120 nm)[12] and the bleed-through of the long-wavelength tail of supercontinuum into fiber anomalous dispersion regime (>1250 nm, Table S3 in the Supplementary Material) would not degrade single-mode coherent supercontinuum generation. Also silica photonic crystal fibers with even larger cores, e.g., 100 μm (SC-1500/100-Si-ROD, NKT Photonics),[43] may further increase the peak power for supercontinuum generation and the resulting FNWC output while restricting the LPFG-based photodamage. Finally, the improvement of hollow-core delivery fibers on single-mode low-loss transmission,[44] bending tolerance, and polarization maintenance may continue.

The unique fiber delivery of spectrally filtered fiber supercontinuum pulses excels at user-friendly and cost-effective operation. First, for pulse parameters (λ, f, and τ) of choice, spectrally monitoring the corresponding deterministically generated fiber

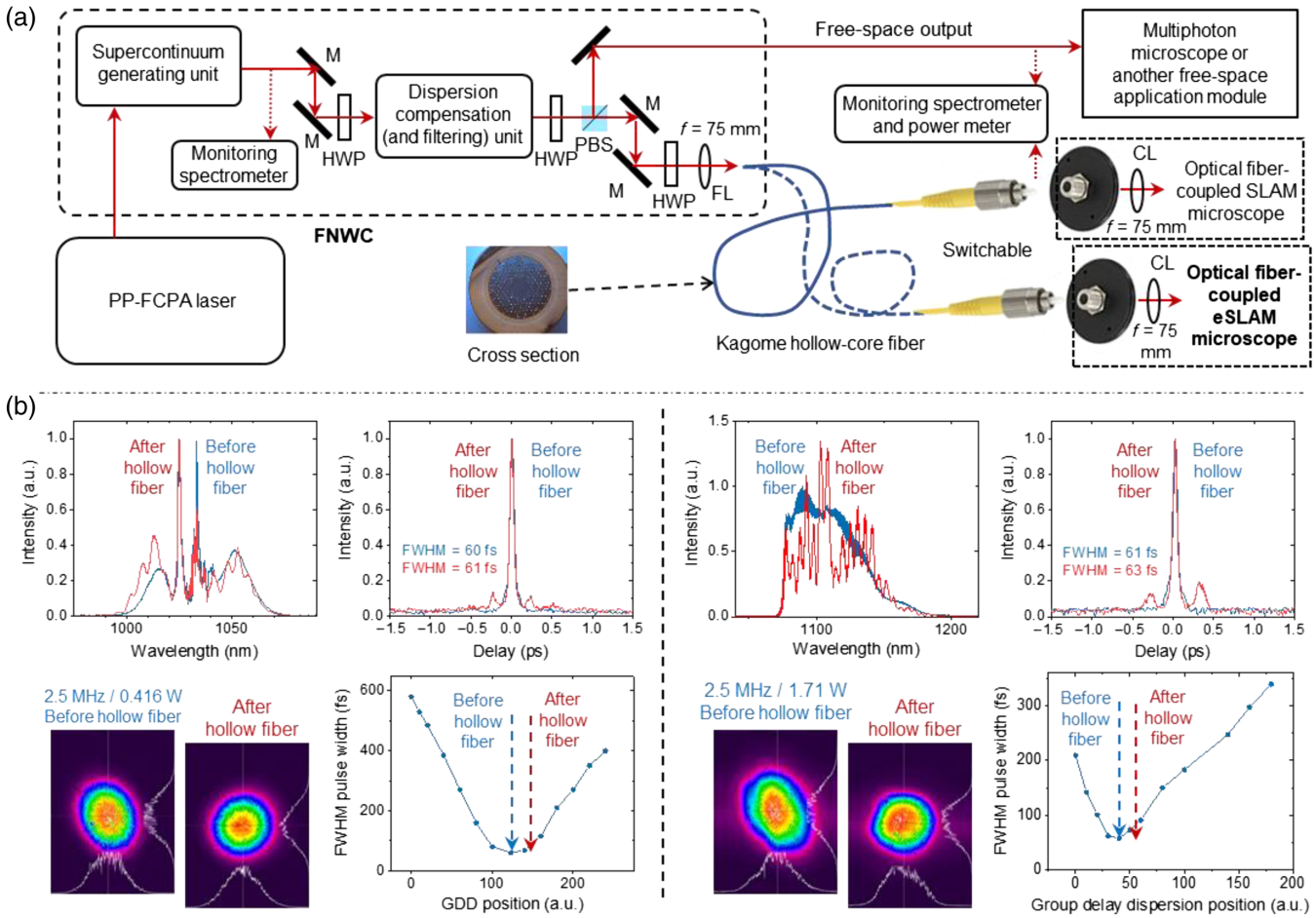

Fig. 2 (a) Schematics of FNWC and related optical components for fs biophotonics switchable between different microscopes (or applications) by fiber-optic telecommunication connection and disconnection. (b) FNWC output spectrum (1030-nm central wavelength without filtering the supercontinuum), pulse width, spatial mode/profile, and full width at half-maximum (FWHM) pulse width versus GDD position before and after 1-m Kagome hollow-core fiber (left), in compassion to FNWC output spectrum (1110-nm central wavelength from filtered supercontinuum), pulse width, spatial mode/profile, and FWHM pulse width versus GDD position before and after 1-m Kagome hollow-core fiber (right).

supercontinuum ensures day-to-day reproducible optical alignment before the FNWC [Fig. 1(a)]. Second, for a preselected spectrum of fiber supercontinuum, monitoring the corresponding fiber delivery output spectrum, power (and plausibly PER), and modal content[45] ensures day-to-day reproducible optical alignment before the application modules [Fig. 2(a)]. Third, the fiber-optic telecommunication-based connection and disconnection of the delivery fiber not only ensures the benefit of laser–microscope alignment decoupling[29] but also enables simple switching or sharing of an integrated PP-FCPA-FNWC laser among different microscopes or applications [Fig. 2(a)].

2.5 Utility in High-Performance Label-Free Multiphoton Microscopy

To test the FNWC in laser-scanning multiphoton microscopy,[46] which is known for overall good performance in 3D sectioning ability, molecular sensitivity/specificity (via fluorescence), and image content (e.g., field of view, spatial resolution, and depth). We replaced the supercontinuum source (Table S3 in the Supplementary Material, Scheme 1) of our simultaneous label-free autofluorescence multiharmonic (SLAM) microscope[47] with the FNWC (Table S3 in the Supplementary Material, Scheme 3) and collimated the fiber-delivered pulses by an achromatic lens as a free-space beam input to the microscope [Fig. 2(a)]. By operating the FNWC at the optimized illumination of SLAM imaging that integrates four modalities of two- and three-photon excited autofluorescence and harmonics (2PAF, SHG, 3PAF, and THG; see Table 1), we reliably visualize live samples, such as *ex vivo* rodent tissue (Fig. S1 in the Supplementary Material). The plausible high-order mode coupling and related side-pulse generation [Fig. 2(b)] in the delivery fiber did not degrade the imaging performance, as also demonstrated in multiphoton microscopy with Kagome hollow-core fiber delivery of Ti:sapphire laser pulses.[48] However, the FNWC retains stable output after > 2000 h (and counting) of cumulative operation without replacing the supercontinuum generating photonic crystal fiber, overcoming a critical limitation of the original SLAM

Table 1 Complementary features of regular SLAM imaging and eSLAM imaging that share one FNWC.

	Regular SLAM	eSLAM
Pulse repetition rate (average power)	10 MHz ($\leq$ 17 mW[a]) on sample	5 MHz ($\leq$ 17 mW[a]) on sample
Photonic crystal fiber (lifetime)	LMA-PM-15, NKT Photonics (~100 h)	LMA-PM-40-FUD, NKT Photonics (> 2000 h)
Optical scanner; fast-axis line rate	Galvo–Galvo (6215 H, Cambridge Technology); up to 350 Hz	Resonant (SC30, Electro-Optical Products) and Galvo (GVS011, Thorlabs); 1592 Hz
Pulse number per pixel per frame	50 to 120	1
Photodetection mode	Photon counting	Analog sampling (2 GHz for 2PF/3PF; 125 MHz for SHG/THG)
PMT1-THG, quantum efficiency	H7421-40 (Hamamatsu), 20.4%	H10721-210 (Hamamatsu), 42.4%
PMT2-3PAF, quantum efficiency	H7421-40 (Hamamatsu), 31.8%	H7422A-40 (Hamamatsu), 42.1%
PMT3-SHG, quantum efficiency	H7421-40 (Hamamatsu), 33.4%	H10721-20 (Hamamatsu), 16.8%
PMT4-2PAF, quantum efficiency	H7421-40 (Hamamatsu), 31.6%	H7422A-40 (Hamamatsu), 41.4%
Peak quantum efficiency wavelength of PMT	H7421-40: 580 nm	H7422A-40: 580 nm H10721-20: 630 nm H10721-210: 400 nm
Frame size (field of view)	700 pixel × 700 pixel ($\leq$ 300 μm × 300 μm)	1024 pixel × 1024 pixel (250 μm × 250 μm)
Pixel dwell time (μs) (pulses/pixel/frame)	2 to 10 (20 to 100)	0.2 (1)
Frame illumination/acquisition time (s)	1 to 5	0.33/1.37
Average output power after pulse shaper (mW)	50	200
Raw data acquisition for real-time display and storage	Enabled by a regular CPU	Enabled by a GPU (GeForce RTX 2080, NVIDIA)
Strength	Low detection noise and flexible optical scanning	High temporal resolution with FLIM capability
Weakness	Low temporal resolution that would be worsened by FLIM	Large detection noise and inflexible optical scanning
Suitable application	Quantitative live-cell imaging for drug discovery, label-free imaging with weak signals, small-scale optical biopsy, etc.	Imaging dynamically moving live samples, label-free imaging with moderate signals, labeled imaging, large-scale optical biopsy, etc.

[a]Limited by phototoxicity. Common features: illumination band: $1110\ \text{nm} \pm 30\ \text{nm}$; pulse width on sample: 60 fs (FWHM); microscope objective; UAPON40XW340 (Olympus), NA 1.15 water immersion.

microscope. Beyond regular SLAM imaging with long-term stability, FNWC can adapt to evolving research needs, such as high temporal-resolution intravital imaging and high-throughput fluorescence lifetime imaging microscopy (FLIM), by tuning the illumination (i.e., repetition rate from 10 to 5 MHz) and building an extended SLAM microscope (eSLAM, Fig. S2 in the Supplementary Material) with a fiber-coupled input [Fig. 2(a)]. We replaced the slow flexible optical scanner and four photon-counting photomultipliers in the SLAM microscope with a fast inflexible scanner and four analog-detection photomultipliers that enabled FLIM via single-photon peak event detection[49] (Table 1). The mode-locking electronic signal was used as the master clock to synchronize optical scanning and subsequent signal acquisition.

The increased speed of eSLAM over regular SLAM imaging lowered the excitation cycle to the minimum of 1 pulse per pixel per frame (Table 1), and thus limited the signal-to-noise ratio (SNR) in the intravital imaging of a mouse skin flap (Video 1) with THG-visible flowing blood cells [Fig. 3(a), arrows] along with SHG-visible collagen fibers and periodic sarcomeres along muscle myofibrils[50] [Fig. 3(a), arrowhead]. This low SNR is often encountered in real-time nonlinear optical imaging free of labeling and phototoxicity. With the advent of modern machine-learning models such as DeepCAD-RT,[51] the SNR can be improved considerably (Video 2), but at the cost of the ability to track individual blood cells [Fig. 3(b), arrows] and resolve the periodic sarcomeres [Fig. 3(b), arrowhead]. In sharp contrast, another machine-learning model known as UDVD[52] not only improves the SNR considerably but also recovers this ability [Fig. 3(c), arrows and arrowheads; Video 3], indicating its better suitability for our intravital imaging of dynamically moving samples. For weaker 2PAF/3PAF signals collected simultaneously, UDVD reveals 2PAF-visible stromal cells [Fig. 3(d), arrows] and 3PAF-visible lipids [Fig. 3(d), stars] barely discernible in the raw data [Fig. 3(e)], exhibiting a larger SNR improvement in comparison to the SHG/THG signals (Fig. S3 in the Supplementary Material). Also, in two different instances of imaging, UDVD unambiguously reveals the presence of

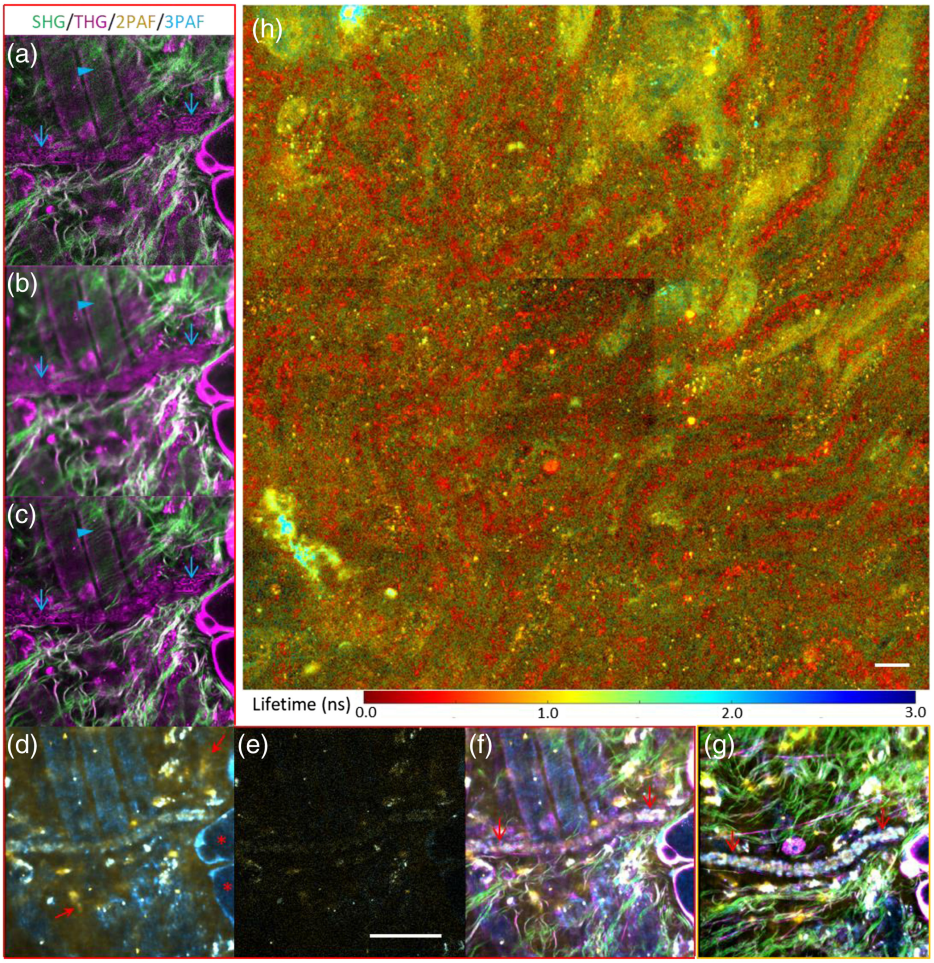

Fig. 3 FLIM-empowered eSLAM imaging of unlabeled live specimens by FNWC. Scale bar: 50 μm. (a)–(g) Time-lapse intravital imaging of a surgically opened mouse skin flap at one instance, showing flowing blood cells in a blood vessel (cyan arrows) and periodic sarcomeres along muscle myofibrils (arrowhead) in raw SHG/THG data (a) which are blurred in DeepCAD-RT-denoised data with a better overall SNR (b) but recovered in UDVD-denoised data with a better overall SNR (c); the UDVD-denoised data (d) also reveal stromal cells (red arrows) and lipids (stars) barely visible in raw 2PAF/3PAF data (e), resulting in a composite four-color image with discernible blood cells at one instance (f) that can be compared with the similar image at a different instance (g) (see Video 3). (h) 2PAF lifetime (FLIM) image of *ex vivo* mouse kidney tissue over a 5×5 mosaic of fields of view (1 mm^2 total area) that shows the red-colored large-scale vasculature with a fluorescence lifetime of <0.6 ns.

intracellular 2PAF, 3PAF, and THG signals in different parts of single biconcave disk-shaped blood cells [Figs. 3(f) and 3(g), arrows; Fig. S4 in the Supplementary Material versus Video 1], which can be confirmed by imaging a fresh blood smear sample (Fig. S5 in the Supplementary Material). In fact, UDVD benefits all instances of time-lapse eSLAM imaging despite the inevitable sample movement during the imaging (Video 3 versus Video 1). Therefore, the FNWC source can enable real-time visualization of fast biological processes, ensured by the robust, long-lifetime PCF for long-term reliability. Furthermore, tunable parameters including repetition rate, pulse duration, wavelength, and power empower users to identify optimal imaging conditions that maximize the signal-to-photodamage ratio for their unique applications.[53]

To demonstrate the high throughput of eSLAM imaging with its built-in FLIM ability in live-tissue pathology, we collected THG [Fig. S6(a) in the Supplementary Material], SHG [Fig. S6(b) in the Supplementary Material], 3PAF intensity [Fig. S6(c) in the Supplementary Material], 3PAF lifetime [Fig. S6(d) in the Supplementary Material], 2PAF intensity [Fig. S6(e) in the Supplementary Material], and 2PAF lifetime [Fig. S6(f) in the Supplementary Material] images from a large area (1 mm^2) of *ex vivo* mouse kidney tissue in 30 min. All images involved a 5×5 mosaic of fields of view with an overlapping factor of 20%, which was enabled by an automatic mechanical stage. Among these images, only 2PAF lifetime unambiguously reveals the large-scale vasculature expected from vital kidney tissue that has been visualized at a typical 250 μm $\times$ 250 μm field of view[54] [Fig. 3(h), Fig. S6(f) in the Supplementary Material]. It should be noted that some elongated patterns of punctuated points in the 2PAF intensity image [Fig. S6(e) in the Supplementary Material, arrows] do not

co-register with red-colored vasculature in the 2PAF lifetime image [Fig. S6(f) in the Supplementary Material]. Similar large-scale data in a 3D volume were obtained in 12 min to reveal the depth-resolved vasculature (Video 4). It is conceivable that this high-content imaging by FLIM-included eSLAM may help pathologists diagnose diseases from fresh core biopsies or surgical specimens (optical biopsy).

3 Discussion and Conclusion

Our FNWC is not limited to label-free imaging. Due to the relatively high-peak power afforded by this device, its deficiency in two-photon excitation of common fluorophores below 950 nm may be compensated by three-photon excitation across 950 to 1110 nm. More importantly, the tunable aspect of FNWC will enable fast prototyping or optimization of imaging condition not available from alternative lasers.[55] For multiphoton microscopy with photon order n (>1 integer), the signal generation rate scales with $P^n/(f\tau)^{n-1}$. Thus a combined low-f and short-τ excitation condition, i.e., a high duty-cycle inverse $(f\tau)^{-1}$, would enhance the signal at a given P, which is limited by laser safety of American National Standards Institute (ANSI). However, one well-known photodamage mechanism also scales with $P^r/(f\tau)^{r-1}$, in which the nonlinear order r lies between 2 and 3.[56] Given a two-photon signal of interest ($n = 2$), the mitigation of this highly nonlinear ($2 < r < 3$) photodamage demands a low duty-cycle inverse $(f\tau)^{-1}$ because $n < r$. On the other hand, there exists another popular photodamage mechanism that includes two-photon absorption-induced photochemical damage ($r = 2$)[57] and one-photon absorption-induced photothermal damage ($r = 1$).[58] Because $n \geq r$, the mitigation of this low-r photodamage demands a high-duty-cycle inverse. Thus the flexibility in f and τ is needed to optimize the signal-to-photodamage ratio for two-photon microscopy, depending on specific biological samples and photodamage mechanisms. With the advent of modern machine-learning models, such as UDVD and DeepCAD-RT, this optimization should emphasize low photodamage more than a high SNR and can be performed in a user-friendly and cost-effective manner by our tunable FNWC with unique fiber delivery of spectrally filtered fiber supercontinuum pulses. For free-space output, the stable supercontinuum generation by FNWC allows programmable label-free contrast generation for gentle multiphoton microscopy.[29] However, while integrating modern machine-learning models can significantly enhance this optimization process, there are limitations to consider. These include the computational resources required for model training and inference, as well as the potential need for extensive training data to accurately predict optimal conditions across diverse samples. Specific denoising models also come with trade-offs. For instance, UDVD, despite its superior denoising performance, has low training and inference speed due to the pixel-wise prediction process, making it less feasible for real-time processing. Nonetheless, self-supervised denoising approaches, such as those demonstrated in this study, do not rely on high-SNR ground truth for training, making them readily applicable to numerous microscopic video restoration tasks.

The key enabling feature of FNWC is the surprising suppression of the long-term fiber photodamage in coherent supercontinuum generation using a photonic crystal fiber with large-pitch small-hole lattice. With this innovation, one laser source can serve both the regular SLAM and eSLAM microscopes, which complement each other in different imaging applications (Table 1). The primary rationale behind selecting a rather low repetition rate for both imaging systems is that it allows for achieving high peak power in pulses without increasing the average power, thereby reducing potential thermal damage and improving excitation efficiency. Additionally, the choice of specific repetition rates is influenced by the requirements of specific biological applications, such as the necessity for labeling and imaging speed. Once the corresponding optics is prealigned, the switch between the two types of imaging can be done by simple connection and disconnection of optical telecommunication within seconds/minutes [Fig. 2(a), lower right], without any effort of optical realignment. Meanwhile, reproducible laser operation can be ensured by inline monitoring spectrometers and a power meter [Figs. 1(a) and 2(a)]. This unique adaptation to evolving research needs may be extended to nonimaging applications of femtosecond biophotonics, e.g., precision surgery, laser tweezer, and optogenetics,[39] to address the unmet needs of: (i) widely and independently tuned in λ, f, and τ with sufficient P or E; (ii) the extensive use of optical fibers robust against environmental perturbations that permits portable access to tunable ultrafast laser technology outside an environmentally controlled laboratory; and (iii) optical fiber-delivered output that allows safe access to high-irradiance laser pulses by diverse users working in real-world situations (but without extensive laser training).

Finally, we note that various ultrashort pulses have been similarly generated by nonlinear compression based on self-phase modulation in the forms of gas cells,[59] gas-filled hollow-core fibers,[60] and multiplates.[61] Also optical pulses like those present in this study have been produced by gain-managed nonlinear amplification,[62] which has been employed in multiphoton microscopy.[63] We hope that the reported FNWC, with its rather unique tunability in pulse repetition rate, will further expands fs biophotonics to benefit field biologists, neuroscientists, veterinarians, surgeons, and pathologists. The combination of FNWC and AI-assisted single-pulse-per-pixel imaging reflects a conceptual novelty for label-free multiphoton imaging.

4 Appendix A: Methods

4.1 Animal Tissue

All animal procedures were conducted in accordance with protocols approved by the Illinois Institutional Animal Care and Use Committee at the University of Illinois at Urbana-Champaign. Kidney was excised from a rabbit (*Oryctolagus cuniculus*, Charles River Laboratories, Wilmington, Massachusetts, United States), submerged in sterile Ca^{2+}/Mg^{2+}-free 0.1 μm filter-sterilized PBS (pH 7.0 to 7.2) and washed from blood by changing the PBS solution. The kidney was manually sliced in a sterile tissue culture dish kept on ice. Individual tissue slices were then placed onto uncoated 35 mm imaging dishes with No. 0 coverslip and 20 mm glass diameter (MatTek, #P35G-0-20-C). The slices were incubated in 500 μL FluoroBrightTM DMEM (ThermoFisher Scientific, #A1896701) supplemented with 10% FBS, 1% PSA, and 4 mM L-Glutamine solutions. Mice (C57BL/6J, Jackson Laboratory) were used to obtain *ex vivo* kidney samples and blood smear samples, which were imaged directly behind a coverslip in an inverted SLAM/eSLAM microscope without solution-based preparation. Incision to expose mouse mammary tissue and externalization of the skin flap was performed under isoflurane anesthesia. The skin flap was placed on a large coverslip and imaged by

the inverted eSLAM microscope, while the mouse was anesthetized with 1% isoflurane mixed with O_2 at a flow rate of 1 L/min. Throughout the imaging, a heating blanket was used to maintain the physiological temperature. Imaging was limited to 3 h duration, after which the mouse was euthanized.

4.2 Self-Supervised Denoising Models

Two self-supervised denoising models, i.e., DeepCAD-RT and UDVD, were used for eSLAM video denoising. Individual channels (SHG, THG, 2PAF, and 3PAF) of the low-SNR videos were used to train UDVD or DeepCAD-RT separately for 100 epochs. To quantify the noise level for the whole video without noise-free ground truth, we defined SNR as μ/σ, where μ is the mean pixel value and σ is the corresponding standard deviation. SNR was measured across all frames in the original and denoised videos (Fig. S3 in the Supplementary Material). The machine learning was conducted on a workstation computer equipped with a central processing unit (CPU) (Xeon W-2195, Intel), four graphics processing units (GPUs) (RTX 8000, Nvidia), and 256 gigabytes of memory. The workstation operates on the Ubuntu system (version 18.04). DL-based video denoising and data analysis were conducted using Python (version 3.9). PyTorch (version 1.11.0) was used during the implementation of the denoising models. Scikit-learn (version 0.23.2) was used for the calculation of evaluation metrics. Plots were generated using Matplotlib (version 3.2.2) and Seaborn (version 0.11.0). Other Python libraries, including Numpy (version 1.19.1), Pandas (version 1.1.2), and SciPy (version 1.5.2), were used to assist data analysis.

5 Appendix B: Supplementary Information

In addition to the Supplementary Material, the following supplementary videos are included:

Video 1, Time-lapse intravital eSLAM imaging of mouse skin flap without image denoising (MP4, 24.1 MB [URL: https://doi.org/10.1117/1.APN.3.4.046012.s1]).

Video 2, Time-lapse intravital eSLAM imaging of the mouse skin flap denoised by DeepCAD-RT (MP4, 4.98 MB [URL: https://doi.org/10.1117/1.APN.3.4.046012.s2]).

Video 3, Time-lapse intravital eSLAM imaging of the mouse skin flap denoised by UDVD (MP4, 4.83 MB [URL: https://doi.org/10.1117/1.APN.3.4.046012.s3]).

Video 4, Depth-resolved eSLAM imaging of *ex vivo* mouse kidney with SHG/green against THG/magenta contrasts (upper left), 2PAF/yellow against 3PAF/cyan contrasts (lower left), 2PAF lifetime contrast (upper right), and 3PAF lifetime contrast (lower right) (MP4, 10.3 MB [URL: https://doi.org/10.1117/1.APN.3.4.046012.s4]).

Disclosures

Haohua Tu is in discussion with the Office of Technology Management at the University of Illinois at Urbana-Champaign on the commercial potential of the developed technology. Other authors declare no competing interests.

Code and Data Availability

Data underlying the results presented in this paper are within the paper and Supplementary files.

Author Contributions

G.W. and H.T. conceived the idea. G.W. and H.T. conducted the related experiments. G.W., J.S., J.E.S., and R.R.I. performed the data analysis. G.W., J.S., and H.T. drafted the manuscript. H.T. reviewed and edited the manuscript with inputs from all authors.

Acknowledgments

The authors would like to thank Stephen A. Boppart for sharing his laboratory, providing laboratory equipment resources, and mentoring Jindou Shi, Rishyashring R. Iyer, and Janet E. Sorrells, and also to thank Edita Aksamitiene and Eric J. Chaney for preparing biological samples. H.T. acknowledged the financial support from the National Institutes of Health, U.S. Department of Health and Human Services (Grant No. R01 CA241618). J.E.S. and R.R.I were supported by NIBIB/NIH (Award No. T32EB019944).

References

1. U. Keller, "Recent developments in compact ultrafast lasers," *Nature* **424**, 831–838 (2003).
2. M. Gu et al., *Femtosecond Biophotonics: Core Technology and Applications*, Cambridge University Press (2010).
3. A. DeMaria, D. Stetser, and H. Heynau, "Self-mode locking of lasers with saturable absorbers," *Appl. Phys. Lett.* **8**, 174–176 (1966).
4. P. F. Moulton, "Spectroscopic and laser characteristics of Ti:Al_2O_3," *J. Opt. Soc. Am. B* **3**, 125–133 (1986).
5. D. E. Spence, P. N. Kean, and W. Sibbett, "60-fsec pulse generation from a self-mode-locked Ti:sapphire laser," *Opt. Lett.* **16**, 42–44 (1991).
6. D. P. G. Smith and J. Klein, "Taking multiphoton imaging to new depths," https://cdn.komachine.com/media/product-catalog/laser-spectra_108880_nnosms.pdf
7. K. König, "Clinical multiphoton tomography," *J. Biophotonics* **1**, 13–23 (2008).
8. A. Vogel et al., "Mechanisms of femtosecond laser nanosurgery of cells and tissues," *Appl. Phys. B* **81**, 1015–1047 (2005).
9. E. Papagiakoumou, E. Ronzitti, and V. Emiliani, "Scanless two-photon excitation with temporal focusing," *Nat. Methods* **17**, 571–581 (2020).
10. C. Xu and F. Wise, "Recent advances in fibre lasers for nonlinear microscopy," *Nat. Photonics* **7**, 875–882 (2013).
11. D. Strickland and G. Mourou, "Compression of amplified chirped optical pulses," *Opt. Commun.* **55**, 447–449 (1985).
12. NKT Photonics Whitepaper, "Modal properties of the DC-200/40-PZ-Yb LMA fiber," https://www.sevensix.co.jp/wp-content/uploads/WhitePaper_DC-200-40-PZ-Yb-ModalProperties.pdf (2013).
13. G. Cerullo and S. De Silvestri, "Ultrafast optical parametric amplifiers," *Rev. Sci. Instrum.* **74**, 1–18 (2003).
14. R. Alfano and S. Shapiro, "Emission in the region 4000 to 7000 Å via four-photon coupling in glass," *Phys. Rev. Lett.* **24**, 584 (1970).
15. M. K. Reed, M. K. Steiner-Shepard, and D. K. Negus, "Widely tunable femtosecond optical parametric amplifier at 250 kHz with a Ti:sapphire regenerative amplifier," *Opt. Lett.* **19**, 1855–1857 (1994).
16. J. K. Ranka, R. S. Windeler, and A. J. Stentz, "Visible continuum generation in air–silica microstructure optical fibers with anomalous dispersion at 800 nm," *Opt. Lett.* **25**, 25–27 (2000).
17. A. Rulkov et al., "High brightness picosecond all-fiber generation in 525–1800 nm range with picosecond Yb pumping," *Opt. Express* **13**, 377–381 (2005).

18. H. Tu and S. A. Boppart, "Coherent fiber supercontinuum for biophotonics," *Laser Photonics Rev.* **7**, 628–645 (2013).
19. L. E. Hooper et al., "Coherent supercontinuum generation in photonic crystal fiber with all-normal group velocity dispersion," *Opt. Express* **19**, 4902–4907 (2011).
20. S. Domingue and R. Bartels, "Nearly transform-limited sub-20-fs pulses at 1065 nm and >10 nJ enabled by a flat field ultrafast pulse shaper," *Opt. Lett.* **40**, 253–256 (2015).
21. W. Liu et al., "Self-phase modulation enabled, wavelength-tunable ultrafast fiber laser sources: an energy scalable approach," *Opt. Express* **24**, 15328–15340 (2016).
22. S. You et al., "Slide-free virtual histochemistry (Part I): development via nonlinear optics," *Biomed. Opt. Express* **9**, 5240–5252 (2018).
23. L. Xiao et al., "Fusion splicing photonic crystal fibers and conventional single-mode fibers: microhole collapse effect," *J. Lightwave Technol.* **25**, 3563–3574 (2007).
24. Y.-Z. Liu et al., "Simultaneous two-photon activation and imaging of neural activity based on spectral–temporal modulation of supercontinuum light," *Neurophotonics* **7**, 045007 (2020).
25. S. You et al., "Label-free visualization and characterization of extracellular vesicles in breast cancer," *Proc. Natl. Acad. Sci. U. S. A.* **116**, 24012–24018 (2019).
26. H. Tu et al., "Scalar generalized nonlinear Schrödinger equation-quantified continuum generation in an all-normal dispersion photonic crystal fiber for broadband coherent optical sources," *Opt. Express* **18**, 27872–27884 (2010).
27. H. Tu et al., "Nonlinear polarization dynamics in a weakly birefringent all-normal dispersion photonic crystal fiber: toward a practical coherent fiber supercontinuum laser," *Opt. Express* **20**, 1113–1128 (2012).
28. Y. Liu et al., "Suppressing short-term polarization noise and related spectral decoherence in all-normal dispersion fiber supercontinuum generation," *J. Lightwave Technol.* **33**, 1814–1820 (2015).
29. H. Tu et al., "Stain-free histopathology by programmable supercontinuum pulses," *Nat. Photonics* **10**, 534–540 (2016).
30. H. Tu et al., "Localized waveguide formation in germanosilicate fiber transmitting femtosecond IR pulses," *J. Opt. Soc. Am. B* **25**, 274–278 (2008).
31. H. Tu et al., "Photoscattering effect in supercontinuum-generating photonic crystal fiber," *Appl. Phys. Lett.* **92**, 061104 (2008).
32. H. Tu et al., "Emergence of self-organized long-period fiber gratings in supercontinuum-generating optical fibers," *Opt. Lett.* **34**, 668–670 (2009).
33. L. Rindorf et al., "Photonic crystal fiber long-period gratings for biochemical sensing," *Opt. Express* **14**, 8224–8231 (2006).
34. B. Li et al., "Investigation of the long wavelength limit of soliton self-frequency shift in a silica fiber," *Opt. Express* **26**, 19637–19647 (2018).
35. S. Lefrançois et al., "Scaling of dissipative soliton fiber lasers to megawatt peak powers by use of large-area photonic crystal fiber," *Opt. Lett.* **35**, 1569–1571 (2010).
36. K. Charan et al., "Fiber-based tunable repetition rate source for deep tissue two-photon fluorescence microscopy," *Biomed. Opt. Express* **9**, 2304–2311 (2018).
37. B. Xu et al., "Quantitative investigation of the multiphoton intrapulse interference phase scan method for simultaneous phase measurement and compensation of femtosecond laser pulses," *J. Opt. Soc. Am. B* **23**, 750–759 (2006).
38. A. M. Weiner, "Femtosecond pulse shaping using spatial light modulators," *Rev. Sci. Instrum.* **71**, 1929–1960 (2000).
39. K. Paul et al., "Coherent control of an opsin in living brain tissue," *Nat. Phys.* **13**, 1111–1116 (2017).
40. J. T. Kristensen et al., "Low-loss polarization-maintaining fusion splicing of single-mode fibers and hollow-core photonic crystal fibers, relevant for monolithic fiber laser pulse compression," *Opt. Express* **16**, 9986–9995 (2008).
41. T. A. Birks, J. C. Knight, and P. St. J. Russell, "Endlessly single-mode photonic crystal fiber," *Opt. Lett.* **22**, 961–963 (1997).
42. J. Limpert et al., "Extended single-mode photonic crystal fiber lasers," *Opt. Express* **14**, 2715–2720 (2006).
43. B. Li et al., "An adaptive excitation source for high-speed multiphoton microscopy," *Nat. Methods* **17**, 163–166 (2020).
44. F. Amrani et al., "Low-loss single-mode hybrid-lattice hollow-core photonic-crystal fibre," *Light: Sci. Appl.* **10**, 7 (2021).
45. V. Bock et al., "Modal content measurements (S^2) of negative curvature hollow-core photonic crystal fibers," *Opt. Express* **25**, 3006–3012 (2017).
46. W. Denk, J. H. Strickler, and W. W. Webb, "Two-photon laser scanning fluorescence microscopy," *Science* **248**, 73–76 (1990).
47. S. You et al., "Intravital imaging by simultaneous label-free autofluorescence-multiharmonic microscopy," *Nat. Commun.* **9**, 2125 (2018).
48. M. Andreana et al., "Ultrashort pulse Kagome hollow-core photonic crystal fiber delivery for nonlinear optical imaging," *Opt. Lett.* **44**, 1588–1591 (2019).
49. J. E. Sorrells et al., "Single-photon peak event detection (SPEED): a computational method for fast photon counting in fluorescence lifetime imaging microscopy," *Opt. Express* **29**, 37759–37775 (2021).
50. C. Odin et al., "Collagen and myosin characterization by orientation field second harmonic microscopy," *Opt. Express* **16**, 16151–16165 (2008).
51. X. Li et al., "Real-time denoising enables high-sensitivity fluorescence time-lapse imaging beyond the shot-noise limit," *Nat. Biotechnol.* **41**, 282–292 (2023).
52. D. Y. Sheth et al., "Unsupervised deep video denoising," in *Proc. IEEE/CVF Int. Conf. Comput. Vis.* (2021).
53. G. Wang, S. A. Boppart, and H. Tu, "Compact simultaneous label-free autofluorescence multi-harmonic microscopy for user-friendly photodamage-monitored imaging," *J. Biomed. Opt.* **29**, 036501 (2024).
54. K. W. Dunn et al., "Functional studies of the kidney of living animals using multicolor two-photon microscopy," *Amer. J. Physiol.-Cell Physiol.* **283**, C905–C916 (2002).
55. C. Lefort, "A review of biomedical multiphoton microscopy and its laser sources," *J. Phys. D: Appl. Phys.* **50**, 423001 (2017).
56. A. Hopt and E. Neher, "Highly nonlinear photodamage in two-photon fluorescence microscopy," *Biophys. J.* **80**, 2029–2036 (2001).
57. K. König et al., "Pulse-length dependence of cellular response to intense near-infrared laser pulses in multiphoton microscopes," *Opt. Lett.* **24**, 113–115 (1999).
58. B. R. Masters et al., "Mitigating thermal mechanical damage potential during two-photon dermal imaging," *J. Biomed. Opt.* **9**, 1265–1270 (2004).
59. L. Lavenu et al., "Nonlinear pulse compression based on a gas-filled multipass cell," *Opt. Lett.* **43**, 2252–2255 (2018).
60. G. Fan et al., "70 mJ nonlinear compression and scaling route for an Yb amplifier using large-core hollow fibers," *Opt. Lett.* **46**, 896–899 (2021).
61. S. Zhang et al., "Solitary beam propagation in periodic layered Kerr media enables high-efficiency pulse compression and mode self-cleaning," *Light: Sci. Appl.* **10**, 53 (2021).
62. P. Sidorenko, W. Fu, and F. Wise, "Nonlinear ultrafast fiber amplifiers beyond the gain-narrowing limit," *Optica* **6**, 1328–1333 (2019).
63. P. Sidorenko et al., "Evaluation of a gain-managed nonlinear fiber amplifier for multiphoton microscopy," *Biomed. Opt. Express* **14**, 2324–2332 (2023).

Biographies of the authors are not available.